Single-Loop and Composite-Loop Realization of Nonadiabatic Holonomic Quantum Gates in a Decoherence-Free Subspace

Zhennan Zhu,[1,2] Tao Chen,[3] Xiaodong Yang,[1,2] Ji Bian,[1,2] Zheng-Yuan Xue,[3,*] and Xinhua Peng[1,2,4,5,†]

[1] *Hefei National Laboratory for Physical Sciences at the Microscale and Department of Modern Physics, University of Science and Technology of China, Hefei, 230026 Anhui, China*

[2] *CAS Key Laboratory of Microscale Magnetic Resonance, University of Science and Technology of China, Hefei, 230026 Anhui, China*

[3] *Guangdong Provincial Key Laboratory of Quantum Engineering and Quantum Materials, GPETR Center for Quantum Precision Measurement, and School of Physics and Telecommunication Engineering, South China Normal University, Guangzhou, 510006 Guangdong, China*

[4] *Synergetic Innovation Center of Quantum Information and Quantum Physics, University of Science and Technology of China, Hefei, 230026 Anhui China*

[5] *College of Physics and Electronic Science, Hubei Normal University, Huangshi, 435002 Hubei, China*

(Received 12 March 2019; revised manuscript received 3 July 2019; published 13 August 2019)

High-fidelity quantum gates are essential for large-scale quantum computation, which can naturally be realized in a noise-resilient way. Geometric manipulation and decoherence-free subspace encoding are promising ways toward robust quantum computation. Here, by combining the advantages of both strategies, we propose and experimentally realize universal holonomic quantum gates in both a single-loop scheme and a composite scheme, based on nonadiabatic and non-Abelian geometric phases, in a decoherence-free subspace with nuclear magnetic resonance. Our experiment uses only two-body resonant spin-spin interactions and thus is experimental friendly. In particular, we also experimentally verify that the composite scheme is more robust against the pulse errors than the single-loop scheme. Therefore, our experiment provides a promising way toward faithful and robust geometric quantum manipulation.

DOI: 10.1103/PhysRevApplied.12.024024

I. INTRODUCTION

It is generally believed that quantum computers can be more efficient in processing certain hard tasks that cannot be done by their classical counterparts. However, quantum information is very fragile and can be destroyed by the weak environmental induced noises. Meanwhile, imperfect quantum manipulation will also introduce additional errors. Therefore, to achieve high-fidelity quantum manipulation, it is essential to fight against various noises and operation errors.

Geometric phases [1–3] have some built-in noise-resilient features [4–8], which are determined by the global properties of the evolution paths. Therefore, geometric quantum computation [9], where quantum gates are induced by geometric transformations, is a promising candidate to achieve high-fidelity quantum manipulation. Moreover, because of the intrinsic noncommutativity, non-Abelian geometric phases [2] can naturally lead to universal quantum gates (i.e., so-called holonomic quantum computation) [10–13]. However, geometric phases based on adiabatic evolutions are so slow that decoherence will introduce considerable gate errors [14,15]. To deal with this difficulty, nonadiabatic holonomic quantum computation (NHQC) was proposed recently [16–19], where fast holonomic quantum gates can be obtained on the basis of nonadiabatic non-Abelian geometric phases. In addition, elementary quantum operations of NHQC have also been experimentally demonstrated in nuclear magnetic resonance (NMR) [20,21], superconducting circuits [22–24], and electron spins in diamond [25–30]. An alternative approach against decoherence is to use decoherence-free-subspace (DFS) encoding [31–33]. Recently, much effort has been made to combine NHQC with DFS encoding [34–41], which can maintain both the noise resilience of the encoding and the operational robustness of holonomies. However, these schemes generally involve three-body or dispersively induced interactions, which are rather complicated and thus difficult to implement experimentally.

Here we propose and experimentally realize a NHQC scheme in a three-qubit DFS [39,40], based on the

*zyxue83@163.com
†xhpeng@ustc.edu.cn

resonant single-loop scenario [42]. Compared with previous schemes [39,40], our implementation simplifies the gate sequences needed for large-scale algorithms, as it can achieve an arbitrary gate in a single step. The other distinct merit of our proposal is that it involves only resonant two-body interactions of two-level systems, thus leading to fast NHQC in a simplified setup. However, the robustness against systematic errors of the single-loop implementation is still the same as in previous schemes. Then, we move another step further to incorporate the composite-loop technique [43,44] into our implementation, which is achieved by our changing the way of accumulating the geometric phase. In addition, both the single-loop implementation and the composite-loop implementation are experimentally tested. Our experimental comparison between the two implementations shows that the composite-loop implementation can indeed further improve the noise resilience of the implemented holonomic quantum gates. Finally, we emphasize that all the DFS-encoding, single-loop, and composite-loop strategies have not yet been experimentally demonstrated. Therefore, our experiment provides a promising method toward robust geometric quantum computation.

II. SINGLE-LOOP AND COMPOSITE NHQC IN A DFS

To realize NHQC in DFS, three physical qubits are encoded as a logical qubit. This DFS is thus spanned by the single-excitation vectors: $S_1 = \{|100\rangle, |001\rangle, |010\rangle\} = \{|0\rangle_L, |1\rangle_L, |E\rangle_L\}$, where a natural encoding of the logical qubit $|\psi\rangle_L = a|0\rangle_L + b|1\rangle_L$ and $|E\rangle_L$ is an ancillary state of the logical qubit; $|mnk\rangle \equiv |m\rangle_1 \otimes |n\rangle_2 \otimes |k\rangle_3$, with the subscript indicating different physical qubits (q_1, q_2, q_3).

A. Universal single-qubit gates

Firstly, we introduce the construction of universal single-logical-qubit holonomic gates. To realize the dynamic construction of the effective Λ-type Hamiltonian based on DFS encoding [39,40], according to the resonant coupling form between physical qubits, the interaction Hamiltonian we design is $\mathcal{H}_S = \mathcal{H}_1(\Omega_1, \phi_1) + \mathcal{H}_2(\Omega_2, \phi_2)$ with

$$\mathcal{H}_i(\Omega_i, \phi_i) = \frac{\Omega_i}{2}[\cos\phi_i(X_iX_{i+1} + Y_iY_{i+1}) + (-1)^{i+1}\sin\phi_i(X_iY_{i+1} - Y_iX_{i+1})], \quad (1)$$

where $i = 1, 2$ and $\mathcal{H}_i(\Omega_i, \phi_i)$ denotes the interaction Hamiltonian between the q_i and q_{i+1} physical qubits with strength Ω_i and phase ϕ_i; X_i and Y_i denote the Pauli operators for the physical qubit q_i.

Setting $\Omega_1 = \Omega\cos\theta/2$ and $\Omega_2 = \Omega\sin\theta/2$, with $\Omega = \sqrt{\Omega_1^2 + \Omega_2^2}$, and $\theta = 2\tan^{-1}(\Omega_2/\Omega_1)$, as shown in

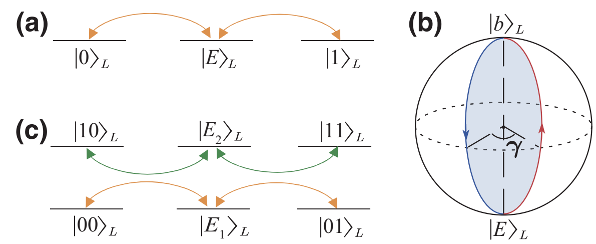

FIG. 1. Proposed setup of our scheme. Effective coupling diagrams for three physical qubits used to realize (a) universal single-logical-qubit gates and (c) nontrivial two-logical-qubit holonomic gates. (b) Geometric illustration of single-logical-qubit gates by the orange-slice-shaped path.

Fig. 1(a), we can write the Hamiltonian $\mathcal{H}_S$ in the DFS S_1 as

$$\mathcal{H}_S = \Omega e^{i\phi_1}\left(\cos\frac{\theta}{2}|0\rangle_L + \sin\frac{\theta}{2}e^{i\phi}|1\rangle_L\right)\langle E| + \text{H.c.} = \Omega e^{i\phi_1}|b\rangle_L\langle E| + \text{H.c.}, \quad (2)$$

where $|b\rangle_L = \cos(\theta/2)|0\rangle_L + \sin(\theta/2)e^{i\phi}|1\rangle_L$, with $\phi = \phi_2 - \phi_1$. In the dressed-state representation $\{|b\rangle_L, |d\rangle_L, |E\rangle_L\}$, the dynamic process of the Hamiltonian $\mathcal{H}_S$ can be regarded as a resonant coupling between the bright state $|b\rangle_L$ and the ancillary state $|E\rangle_L$, while the dark state $|d\rangle_L = \sin(\theta/2)|0\rangle_L - \cos(\theta/2)e^{i\phi}|1\rangle_L$ decouples from the dynamics all the time.

Thereafter, an arbitrary single-logical-qubit holonomic gate in S_1 can be realized with a single-loop scenario by engineering the quantum system to evolve along an orange-slice-shaped path as shown in Fig. 1(b). In our construction, the evolution area is set as $\Omega\tau = \pi$, with τ being the entire evolution time, which is separated into two equal segments. In the second segment $[0, \tau/2]$, we set $\phi_1 = 0$, and then $\mathcal{H}_S$ is reduced to $\mathcal{H}_a = \Omega(|b\rangle_L\langle E| + |E\rangle_L\langle b|)$ and the corresponding evolution operator is $U_a = |d\rangle_L\langle d| - i(|b\rangle_L\langle E| + |E\rangle_L\langle b|)$. In the first segment $[\tau/2, \tau]$, we change the phase ϕ_1 to $\phi_1' = \pi + \gamma$, and then $\mathcal{H}_S = \mathcal{H}_b = -\Omega(e^{i\gamma}|b\rangle_L\langle E| + e^{-i\gamma}|E\rangle_L\langle b|)$ and the corresponding evolution operator $U_b^\gamma = |d\rangle_L\langle d| + i(e^{i\gamma}|b\rangle_L\langle E| + e^{-i\gamma}|E\rangle_L\langle b|)$. In this way, in the logical-qubit computational basis $\{|0\rangle_L, |1\rangle_L\}$, the induced gate operation will be

$$U_S(\gamma,\theta,\phi) = U_b^\gamma U_a = |d\rangle_L\langle d| + e^{i\gamma}|b\rangle_L\langle b| = e^{i(\gamma/2)}\begin{pmatrix} \cos\frac{\gamma}{2} + i\sin\frac{\gamma}{2}\cos\theta & i\sin\frac{\gamma}{2}\sin\theta e^{-i\phi} \\ i\sin\frac{\gamma}{2}\sin\theta e^{i\phi} & \cos\frac{\gamma}{2} - i\sin\frac{\gamma}{2}\cos\theta \end{pmatrix} = e^{i(\gamma/2)}e^{i(\gamma/2)\vec{n}\cdot\vec{\sigma}_L}, \quad (3)$$

where $\vec{\sigma}_L = (X^L, Y^L, Z^L)$ are the Pauli operators for the logical qubit and $\vec{n} = (\sin\theta\cos\phi, \sin\theta\sin\phi, \cos\theta)$. In the Bloch-sphere representation, Eq. (3) indicates a rotation operation around the axis $\vec{n}$ by an angle $\gamma/2$, up to a global phase factor, which can lead to arbitrary single-logical-qubit gates as both $\vec{n}$ and γ are tunable. In addition, the implemented gates are geometric as the evolution of logical-qubit states satisfies (i) the parallel-transport condition, that is, ${}_L\langle j(t)|\mathcal{H}_S|k(t)\rangle_L = 0$, with $j, k \in \{b, d\}$, and (ii) the cyclic evolution condition that is, $|b(\tau)\rangle_L = U_S(\gamma,\theta,\phi)|b\rangle_L = e^{i\gamma}|b\rangle_L$ and $|d(\tau)\rangle_L = U_S(\gamma,\theta,\phi)|d\rangle_L = |d\rangle_L$.

Usually, the existence of systematic errors tends to devastate the advantage of the robustness of holonomic gates in NHQC [45,46]. To overcome this, we suggest implementing the holonomic gates with composite schemes [43,44]. To achieve this in DFS, we take $U_S(\gamma/N,\theta,\phi)$ as an elementary gate, where $N > 1$. Thus, the target gate $U_S(\gamma,\theta,\phi)$ in Eq. (3) can be achieved by sequentially applying the elementary gate N times while keeping the cumulative geometric phase to be γ; that is,

$$[U_S(\gamma/N,\theta,\phi)]^N = U_S(\gamma,\theta,\phi). \tag{4}$$

B. Nontrivial two-qubit gates

We now proceed to the construction of nontrivial two-logical-qubit holonomic gates, combining them with the previously described arbitrary single-logical-qubit holonomic gates. For the two-logical qubit, a six-dimensional DFS exists; that is,

$$\begin{aligned} S_2 &= \{|00\rangle_L, |01\rangle_L, |10\rangle_L, |11\rangle_L, |E_1\rangle_L, |E_2\rangle_L\} \\ &= \{|100100\rangle, |100001\rangle, |001100\rangle, \\ &\quad |001001\rangle, |101000\rangle, |000101\rangle\}, \end{aligned} \tag{5}$$

where $|E_1\rangle_L$ and $|E_2\rangle_L$ are the ancillary states; $|mnkm'n'k'\rangle = |m\rangle_1 \otimes |n\rangle_2 \otimes |k\rangle_3 \otimes |m'\rangle_4 \otimes |n'\rangle_5 \otimes |k'\rangle_6$, that is, the physical qubits (q_1, q_2, q_3) and (q_4, q_5, q_6) encode the first and second logical qubits, respectively. For the two-qubit case, we design the Hamiltonian $\mathcal{H}_T = \mathcal{H}_3 + \mathcal{H}_4$ with

$$\begin{aligned} \mathcal{H}_3 &= \frac{\Omega_3}{2}[\cos\varphi(X_3X_4 + Y_3Y_4) + \sin\varphi(Y_3X_4 - X_3Y_4)], \\ \mathcal{H}_4 &= \frac{\Omega_4}{2}(X_3X_6 + Y_3Y_6). \end{aligned} \tag{6}$$

Defining $\Omega_3 = \Omega'\cos(\vartheta/2)$ and $\Omega_4 = \Omega'\sin(\vartheta/2)$, with $\Omega' = \sqrt{\Omega_3^2 + \Omega_4^2}$, and $\vartheta = 2\tan^{-1}(\Omega_4/\Omega_3)$, we can rewrite $\mathcal{H}_T$ in the DFS S_2 as $\mathcal{H}_T = \mathcal{H}_{LT}^{(1)} + \mathcal{H}_{LT}^{(2)}$, with

$$\mathcal{H}_{LT}^{(1)} = \Omega'\left(e^{-i\varphi}\cos\frac{\vartheta}{2}|00\rangle_L + \sin\frac{\vartheta}{2}|01\rangle_L\right)\langle E_1| + \text{H.c.},$$

$$\mathcal{H}_{LT}^{(2)} = \Omega'\left(e^{i\varphi}\cos\frac{\vartheta}{2}|11\rangle_L + \sin\frac{\vartheta}{2}|10\rangle_L\right)\langle E_2| + \text{H.c.},$$

being two commuting parts. In the subspace $\{|00\rangle_L, |01\rangle_L, |E_1\rangle_L\}$ or $\{|10\rangle_L, |11\rangle_L, |E_2\rangle_L\}$), $\mathcal{H}_{LT}^{(1)}$ or $\mathcal{H}_{LT}^{(2)}$ forms a Hamiltonian that is similar to $\mathcal{H}_S$ in Eq. (2) for the single-logical-qubit gates, and the two subspaces evolve independently with the coupling diagram, as shown in Fig. 1(c). When $\Omega' T = \pi$, with T being the evolution time, the evolution operator in S_2 is

$$U_T(\vartheta,\varphi) = -\begin{pmatrix} \cos\vartheta & \sin\vartheta e^{i\varphi} & 0 & 0 \\ \sin\vartheta e^{-i\varphi} & -\cos\vartheta & 0 & 0 \\ 0 & 0 & -\cos\vartheta & \sin\vartheta e^{i\varphi} \\ 0 & 0 & \sin\vartheta e^{-i\varphi} & \cos\vartheta \end{pmatrix}. \tag{7}$$

As the evolution in the subspace $\{|00\rangle_L, |01\rangle_L\}$ is different from that in the subspace $\{|10\rangle_L, |11\rangle_L\}$ in general, Eq. (7) denotes nontrivial two-qubit gates by our setting different ϑ and/or φ. For example, a controlled-Z gate (U_{CZ}) can be constructed as

$$U_{CZ} = U_S^2\left(\frac{\pi}{2},\frac{\pi}{2},\pi\right) K U_S^2\left(\frac{\pi}{2},\frac{\pi}{2},0\right), \tag{8}$$

with

$$K = U_S^1\left(\pi,\frac{\pi}{2},0\right) U_S^2\left(\pi,\frac{\pi}{4},0\right) U_T\left(\frac{\pi}{4},0\right), \tag{9}$$

where superscripts 1 and 2 label the two logical qubits.

III. EXPERIMENTAL REALIZATIONS

We use diethyl fluoromalonate dissolved in ^{2}H-labeled chloroform at 303 K as a NMR quantum simulator, where three physical qubits (q_1, q_2, q_3) are realized by the nuclear spins of ^{1}H, ^{13}C, and ^{19}F, respectively. The molecular structure and parameters are shown in Fig. 2(a). The natural Hamiltonian in the triple-resonance rotating frame

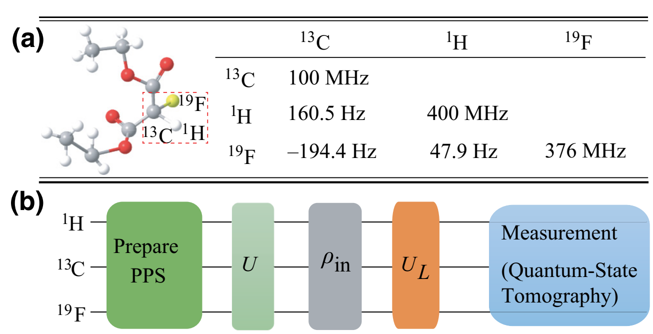

	^{13}C	^{1}H	^{19}F
^{13}C	100 MHz		
^{1}H	160.5 Hz	400 MHz	
^{19}F	–194.4 Hz	47.9 Hz	376 MHz

FIG. 2. (a) Molecular structure and relevant parameters of diethyl fluoromalonate. The chemical shifts and scalar couplings are on and below the diagonal of the table, respectively. (b) Experimental scheme for QPT for different holonomic gates U_L.

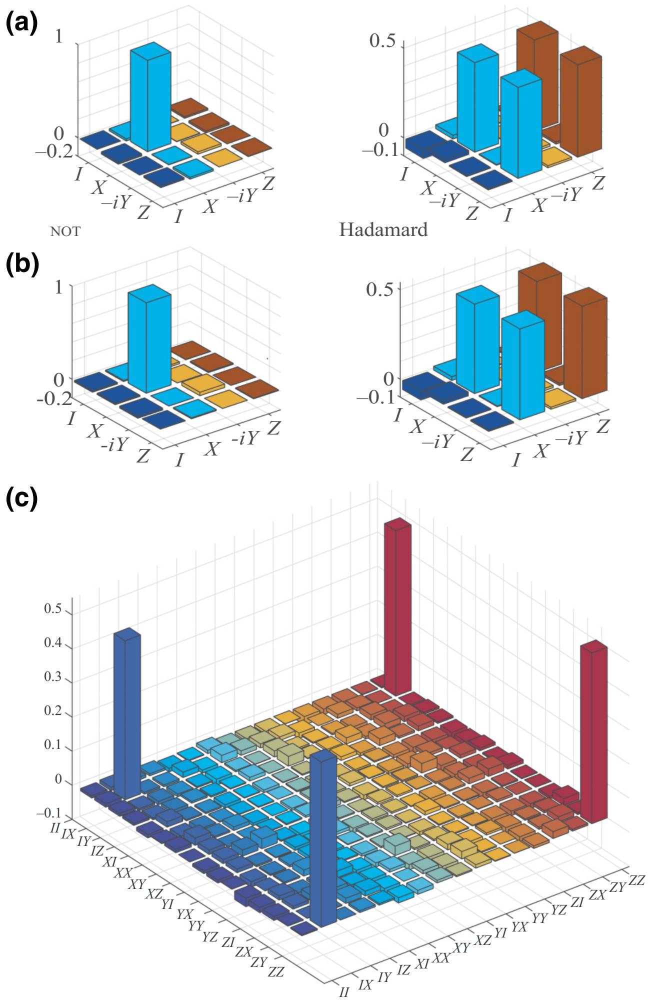

FIG. 3. Experimentally reconstructed χ matrices in the logical-qubit subspace for holonomic gates: (a) NOT (left) and Hadamard (right) gates in the single-loop scheme; that is, NOT $= U_S(\pi, \pi/2, 0)$ and $H = U_S(\pi, \pi/4, 0)$. (b) NOT (left) and Hadamard (right) gates in the composite scheme with $N = 2$; that is, NOT $= [U_S(\pi/2, \pi/2, 0)]^2$ and $H = [U_S(\pi/2, \pi/4, 0)]^2$. (c) A universal two-qubit gate $U_T(\pi/4, 0)$. All the imaginary parts of these χ matrices are less than 0.1, and are not shown here.

is

$$\mathcal{H}_{\text{NMR}} = \frac{\pi}{2} \sum_{1 \le i < j \le 3} J_{ij} Z_i Z_j, \tag{10}$$

where J_{ij} is the scalar coupling strength between the ith nucleus and the jth nucleus. The experiment begins with the preparation of a pseudopure state $\rho_{\text{PPS}} = (1 - \varepsilon)I/8 + \varepsilon|000\rangle\langle 000|$ from the thermal-equilibrium state by the line-selective method [47]. Here $\varepsilon \approx 10^{-5}$ denotes the polarization and I denotes the 8×8 identity matrix. Thereafter, the DFS-encoded logical states can be obtained by the rotations $R_x^1(\pi)|000\rangle = |100\rangle \equiv |0\rangle_L$ and $R_x^3(\pi)|000\rangle = |001\rangle \equiv |1\rangle_L$.

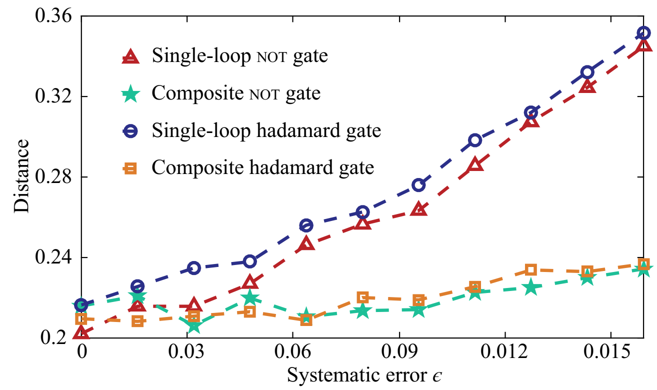

FIG. 4. Experimental gate distances with respect to systematic error ϵ for single-logical-qubit holonomic NOT and Hadamard gates in the single-loop scheme and in the composite scheme with $N = 2$.

In the following, we take holonomic NOT and Hadamard (H) gates as two typical examples of single-logical-qubit gates to experimentally demonstrate their performance. Without loss of generalization, we set $\phi = \phi_2 - \phi_1 = 0$. According to Eq. (3), one can obtain NOT $= U_S(\pi, \pi/2, 0)$ under the evolution of

$$\mathcal{H}_S^N = \mathcal{H}_a^N = \mathcal{H}_b^N = \frac{\sqrt{2}\Omega}{4}[(X_1X_2 + Y_1Y_2 + X_2X_3 + Y_2Y_3)], \tag{11}$$

with duration $\tau = \pi/\Omega$, and $H = U_S(\pi, \pi/4, 0)$ under the evolution of

$$\mathcal{H}_S^H = \mathcal{H}_a^H = \mathcal{H}_b^H = \frac{\Omega}{2}\cos\left(\frac{\pi}{8}\right)(X_1X_2 + Y_1Y_2) + \frac{\Omega}{2}\sin\left(\frac{\pi}{8}\right)(X_2X_3 + Y_2Y_3), \tag{12}$$

with duration τ, in a single-loop scheme. Similarly, according to Eq. (4), composite-pulse implementations are NOT $= [U_S(\pi/2, \pi/2, 0)]^2$ with

$$\mathcal{H}_a^{2N} = \frac{\sqrt{2}\Omega}{4}[(Y_1Y_2 + X_1X_2 + X_2X_3 + Y_2Y_3)],$$
$$\mathcal{H}_b^{2N} = \frac{\sqrt{2}\Omega}{4}[(Y_1X_2 - X_1Y_2 + X_2Y_3 - Y_2X_3)], \tag{13}$$

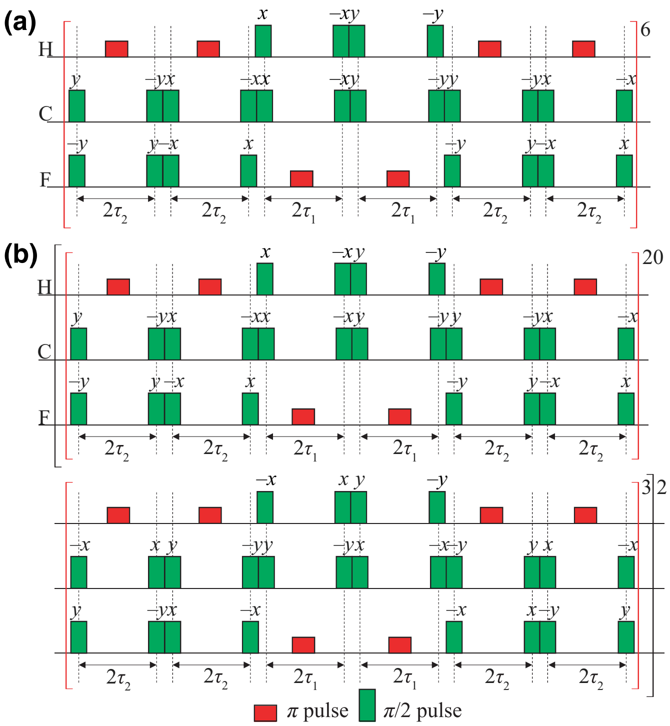

FIG. 5. Experimental pulse sequences for the single-logical-qubit gates $U_S(\pi,\theta,0)$ realized (a) in a single-loop scheme and (b) in a composite scheme with $N=2$. The free evolution times $\tau_1=\cos\frac{\theta}{2}/(12J_{\text{C-H}})$ and $\tau_2=\sin\frac{\theta}{2}/(24J_{\text{C-F}})$.

and $H=[U_S(\pi/2,\pi/4,0)]^2$ with

$$\begin{aligned}\mathcal{H}_a^{2H}=&\frac{\Omega}{2}\cos\left(\frac{\pi}{8}\right)(Y_1Y_2+X_1X_2)\\&+\frac{\Omega}{2}\sin\left(\frac{\pi}{8}\right)(X_2X_3+Y_2Y_3)],\\ \mathcal{H}_b^{2H}=&\frac{\Omega}{2}\cos\left(\frac{\pi}{8}\right)(Y_1X_2-X_1Y_2)\\&+\frac{\Omega}{2}\sin\left(\frac{\pi}{8}\right)(X_2Y_3-Y_2X_3),\end{aligned}\tag{14}$$

for $N=2$. For simplicity, we use the effective coupling parameter $\Omega=1$ in the Hamiltonian $\mathcal{H}_S$ hereafter. Using the Trotter formula, we approximately generate the evolution operator

$$e^{-i\mathcal{H}_S\tau}\cong\left(e^{-i\mathcal{H}_2\frac{\tau}{6}}e^{-i\mathcal{H}_1\frac{\tau}{3}}e^{-i\mathcal{H}_2\frac{\tau}{6}}\right)^3+O\left[\left(\frac{\tau}{3}\right)^3\right].\tag{15}$$

All the gate fidelities can reach 0.9999 by the Trotter approximations; the corresponding pulse sequences are presented in Appendix A.

To quantitatively access experimental implementations of the NHQC gates, we use standard quantum-process tomography (QPT) [48] in the logical-qubit subspace; the experimental scheme is shown in Fig. 2(b) (see Appendix B for details). For single-logical-qubit gates, we prepare the initial state ρ_{in} as $|0\rangle_L,|1\rangle_L,(|0\rangle_L+|1\rangle_L)/\sqrt{2}$ and $(|0\rangle_L+i|1\rangle_L)/\sqrt{2}$ through the operation U, and then perform holonomic operation U_L for different logical gates (e.g., NOT or Hadamard), and finally the output state $\rho_f=U_L\rho_{\text{in}}U_L^\dagger$ is determined by quantum-state tomography [49]. The required information is selected to reconstruct quantum channels in the logical-qubit subspace. The experimentally reconstructed χ matrices in the logical-qubit subspace for holonomic NOT and Hadamard gates are shown in Fig. 3(a) for the single-loop scheme and in Fig. 3(b) for the composite scheme. Here we estimate the quality of the reconstructed gates by the distance between the experimental and theoretical χ matrices under the definition of the Frobenius norm [50]; that is, $D(\chi)\equiv D(\chi_{\text{expt}},\chi_{\text{th}})=\|\chi_{\text{expt}}-\chi_{\text{th}}\|$. The results are 0.202 and 0.217, respectively, for holonomic NOT and Hadamard gates in the single-loop scheme and 0.216 and 0.210, respectively, for holonomic NOT and Hadamard gates in the composite scheme. These errors come mainly from the imperfection of state preparation and measurement (see Appendix C for details).

For the realization of the two-logical-qubit gates, only three physical qubits (q_3,q_4,q_6) are active in the Hamiltonian $\mathcal{H}_T$. Therefore, the dynamics of the two-logical-qubit gates can be simulated with a three-qubit quantum processor. If we ignore the three uninvolved physical qubits, the reduced two-logical-qubit states are

$$\begin{aligned}&|00\rangle_L\Rightarrow|010\rangle_{346},\quad|01\rangle_L\Rightarrow|001\rangle_{346},\\&|10\rangle_L\Rightarrow|110\rangle_{346},\quad|11\rangle_L\Rightarrow|101\rangle_{346},\\&|E_1\rangle_L\Rightarrow|100\rangle_{346},\quad|E_2\rangle_L\Rightarrow|011\rangle_{346}.\end{aligned}\tag{16}$$

In our experiment, the nuclear spins (^{1}H, ^{13}C, ^{19}F) are chosen as physical qubits (q_4,q_3,q_6). Similarly to the case of a single-logical-qubit gate, a two-logical-qubit gate $U_T(\pi/4,0)$ can also be implemented under the evolution of $\mathcal{H}_T=\Omega'[\cos(\pi/8)(X_3X_4+Y_3Y_4)+\sin(\pi/8)(X_3X_6+Y_3Y_6)]/2$ with duration $T=\pi/\Omega'$, where $\Omega'=1$ for simplicity. We perform the standard QPT for two-logical-qubit gates in the logical-qubit subspace by preparing 16 initial states $\{|0\rangle_L,|1\rangle_L,(|0\rangle_L+|1\rangle_L)/\sqrt{2},(|0\rangle_L+i|1\rangle_L)/\sqrt{2}\}\otimes\{|0\rangle_L,|1\rangle_L,(|0\rangle_L+|1\rangle_L)/\sqrt{2},(|0\rangle_L+i|1\rangle_L)/\sqrt{2}\}$. Therefore, the χ matrix for the two-logical-qubit gate $U_T(\pi/4,0)$ can be experimentally determined, as shown in Fig. 3(c), and the gate distance between the experimental and theoretical matrices is 0.274.

IV. ROBUSTNESS TEST

In the following, we experimentally test the robustness of nonadiabatic holonomic quantum gates by taking the single-logical-qubit gates as examples. To do this, we add systematic errors in the Hamiltonian $\mathcal{H}_S$ as $(1+\epsilon)\Omega$, with

ϵ being the error fraction (i.e., the deviation of the coupling strength). This type of error might be caused by the imperfection of π-evolution condition such that the cyclic evolution is no longer satisfied. Using the same QPT procedure as above, we obtain the gate distances versus the error fraction ϵ for nonadiabatic holonomic quantum gates in both the single-loop scheme and the composite scheme, as shown in Fig. 4. The results indicate that holonomic gates realized by the composite scheme have greater robustness against the systematic error ϵ. The abnormal behaviors in the small-systematic-error range for the NOT gate are mainly due to the imperfection of the state preparation and measurement, which dominates the main errors when ϵ is small. In addition, the gate infidelity induced by the initial-state preparation can be further suppressed [51].

V. SUMMARY

By combining the advantages of geometric manipulation and DFS encoding, we propose an extended NQHC scheme, and demonstrate its feasibility in proof-of-principle experiments via a NMR quantum-information processor. We experimentally demonstrate universal NHQC in DFS for both the single-loop scheme and the composite scheme, which is an important step toward fault-tolerant quantum computing. Moreover, we also test the robustness of our implemented gates and show that the holonomic gates realized in the composite scheme have greater robustness against the systematic error than those realized in the single-loop scheme.

ACKNOWLEDGMENTS

This work was supported by the National Key Research and Development Program of China (Grants No. 2018YFA0306600 and No. 2016YFA0301803), the National Natural Science Foundation of China (Grants No. 11425523, No. 11661161018, and No. 11874156), the Key R&D Program of Guangdong Province (Grant No. 2018B030326001), and the Anhui Initiative in Quantum Information Technologies (Grant No. AHY050000).

Z. Zhu and T. Chen contributed equally to this work.

APPENDIX A: EXPERIMENTAL PULSE SEQUENCES

Starting from the Hamiltonian for constructing holonomic quantum gates in Eq. (1), as expected, the target interaction Hamiltonian in experiments we want to design is

$$\begin{aligned}\mathcal{H}_S(\Omega,\theta,\phi;\phi_1) &= \mathcal{H}_S(\Omega_1,\phi_1;\Omega_2,\phi_2) = \sum_{i=1}^{2}\mathcal{H}_i(\Omega_i,\phi_i)\\ &= \frac{\Omega}{2}\left\{\cos\frac{\theta}{2}[\cos\phi_1(X_1X_2+Y_1Y_2)\right.\\ &\quad+\sin\phi_1(X_1Y_2-Y_1X_2)]\\ &\quad+\sin\frac{\theta}{2}[\cos(\phi_1+\phi)(X_2X_3+Y_2Y_3)\\ &\quad\left.-\sin(\phi_1+\phi)(X_2Y_3-Y_2X_3)]\right\}. \end{aligned} \tag{A1}$$

Then, an arbitrary single-logical-qubit gate

$$U_S(\gamma,\theta,\phi) = e^{-i\mathcal{H}_S(\Omega,\theta,\phi;\gamma+\pi)\frac{\tau}{2}}e^{-i\mathcal{H}_S(\Omega,\theta,\phi;0)\frac{\tau}{2}} \tag{A2}$$

can be achieved in a single-loop scheme by our setting $\Omega=\sqrt{\Omega_1^2+\Omega_2^2}$, $\theta=2\tan^{-1}(\Omega_2/\Omega_1)$, and $\phi=\phi_2-\phi_1$,

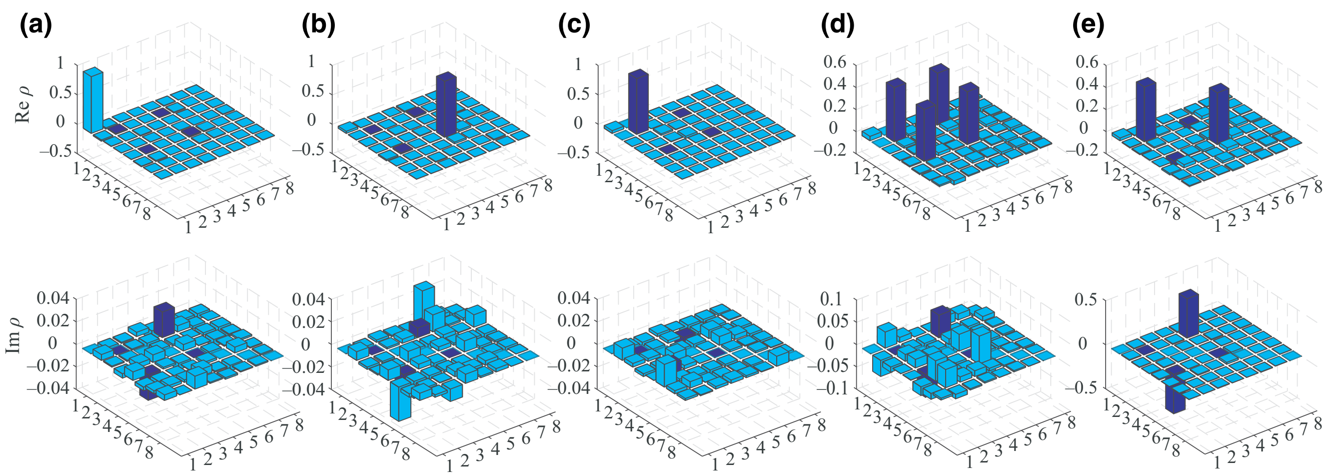

FIG. 6. Experimentally reconstructed density matrices of initial states for single-logical-qubit gates: (a)–(e) correspond to $|000\rangle$, $|0\rangle_L$, $|1\rangle_L$, $(|0\rangle_L+|1\rangle_L)/\sqrt{2}$,and $(|0\rangle_L+i|1\rangle_L)/\sqrt{2}$, respectively, where the elements in the logical-qubit subspace S_1 are marked as dark-blue bars.

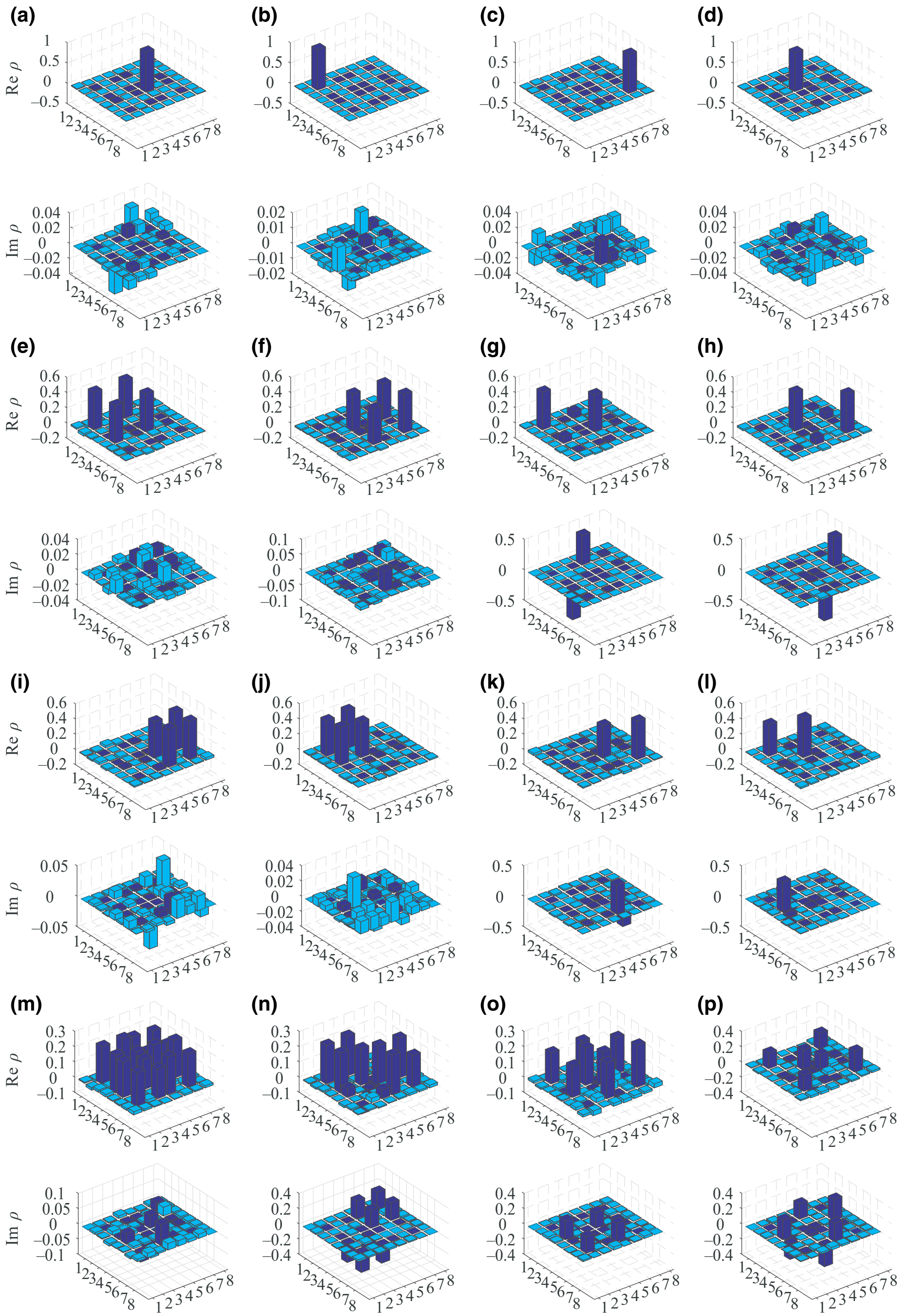

FIG. 7. Experimentally reconstructed density matrices of initial states for two-logical-qubit gates: (a)–(p) respectively correspond to $|00\rangle_L$, $|01\rangle_L$, $|10\rangle_L$, $|11\rangle_L$, $|00\rangle_L + |01\rangle_L)/\sqrt{2}$, $(|10\rangle_L + |11\rangle_L)/\sqrt{2}$, $(|00\rangle_L + i|01\rangle_L)/\sqrt{2}$, $(|10\rangle_L + i|11\rangle_L)/\sqrt{2}$, $(|00\rangle_L + |10\rangle_L)/\sqrt{2}$, $(|01\rangle_L + |11\rangle_L)/\sqrt{2}$, $(|00\rangle_L + i|10\rangle_L)/\sqrt{2}$, $(|01\rangle_L + i|11\rangle_L)/\sqrt{2}$, $(|00\rangle_L + |10\rangle_L + |01\rangle_L + |11\rangle_L)/2$, $(|00\rangle_L + i|01\rangle_L + |10\rangle_L + i|11\rangle_L)/2$, $(|00\rangle_L + i|10\rangle_L + |01\rangle_L + i|11\rangle_L)/2$, and $(|00\rangle_L + i|01\rangle_L + i|10\rangle_L - |11\rangle_L)/2$, where the elements in the two-logical-qubit subspace S_2 are marked as dark-blue bars.

TABLE I. Distances of all initial states experimentally reconstructed. $D(C) = \|C\| = \sqrt{\mathrm{Tr}(CC^T)}$ is the matrix F norm of the matrix C defined by $C = C_{\mathrm{expt}} - C_{\mathrm{th}}$ to quantify the closeness of the experimental matrix C_{expt} and the theoretical matrix C_{th}, where C^T is the conjugate transpose of C. Subscripts F and L denote the three-physical-qubit space and the logical-qubit subspace, respectively.

Order	Logical qubit	Physical qubit (^{1}H,^{13}C,^{19}F)	D_F^I	D_L^I
1	$\|0\rangle_L$	$\|100\rangle$	0.070	0.055
2	$\|1\rangle_L$	$\|001\rangle$	0.072	0.060
3	$\|+\rangle_L$	$(\|100\rangle + \|001\rangle)/\sqrt{2}$	0.147	0.114
4	$\|-\rangle_L$	$(\|100\rangle + i\|001\rangle)/\sqrt{2}$	0.164	0.149
5	$\|00\rangle_L$	$\|100\rangle$	0.070	0.056
6	$\|01\rangle_L$	$\|001\rangle$	0.072	0.063
7	$\|10\rangle_L$	$\|110\rangle$	0.101	0.077
8	$\|11\rangle_L$	$\|011\rangle$	0.113	0.086
9	$(\|00\rangle_L + \|01\rangle_L)/\sqrt{2}$	$(\|100\rangle + \|001\rangle)/\sqrt{2}$	0.147	0.128
10	$(\|10\rangle_L + \|11\rangle_L)/\sqrt{2}$	$(\|110\rangle + \|011\rangle)/\sqrt{2}$	0.187	0.170
11	$(\|00\rangle_L + i\|01\rangle_L)/\sqrt{2}$	$(\|100\rangle + i\|001\rangle)/\sqrt{2}$	0.164	0.155
12	$(\|10\rangle_L + i\|11\rangle_L)/\sqrt{2}$	$(\|110\rangle + i\|011\rangle)/\sqrt{2}$	0.186	0.164
13	$(\|00\rangle_L + \|10\rangle_L)/\sqrt{2}$	$(\|100\rangle + \|110\rangle)/\sqrt{2}$	0.118	0.082
14	$(\|01\rangle_L + \|11\rangle_L)/\sqrt{2}$	$(\|001\rangle + \|011\rangle)/\sqrt{2}$	0.121	0.081
15	$(\|00\rangle_L + i\|10\rangle_L)/\sqrt{2}$	$(\|100\rangle + i\|110\rangle)/\sqrt{2}$	0.115	0.088
16	$(\|01\rangle_L + i\|11\rangle_L)/\sqrt{2}$	$(\|001\rangle + i\|011\rangle)/\sqrt{2}$	0.130	0.101
17	$(\|00\rangle_L + \|01\rangle_L + \|10\rangle_L + \|11\rangle_L)/2$	$(\|100\rangle + \|001\rangle + \|110\rangle + \|011\rangle)/2$	0.190	0.169
18	$(\|00\rangle_L + i\|01\rangle_L + \|10\rangle_L + i\|01\rangle_L)/2$	$(\|100\rangle + i\|001\rangle + \|110\rangle + i\|011\rangle)/2$	0.152	0.135
19	$(\|00\rangle_L + \|01\rangle_L + i\|10\rangle_L + i\|11\rangle_L)/2$	$(\|100\rangle + \|001\rangle + i\|110\rangle + i\|011\rangle)/2$	0.198	0.151
20	$(\|00\rangle_L + i\|01\rangle_L + i\|10\rangle_L - \|11\rangle_L)/2$	$(\|100\rangle + i\|001\rangle + i\|110\rangle - \|011\rangle)/2$	0.169	0.144

with $\Omega\tau = \pi$. For the NOT and Hadamard gates, the operator has the form

$$U_S(\pi,\theta,0) = e^{-i\mathcal{H}_S(\Omega,\theta,0;2\pi)(\tau/2)}e^{-i\mathcal{H}_S(\Omega,\theta,0;0)(\tau/2)} = e^{-i\mathcal{H}_S(\Omega,\theta,0;0)\tau} \quad \text{(A3)}$$

because $\mathcal{H}_S(\Omega,\theta,0;2\pi) = \mathcal{H}_S(\Omega,\theta,0;0) = \Omega[\cos(\theta/2)(X_1X_2 + Y_1Y_2) + \sin(\theta/2)(X_2X_3 + Y_2Y_3)]/2$. The holonomic NOT and Hadamard gates correspond to $\theta = \pi/2$ and $\pi/4$, respectively.

Using the Trotter formula in Eq. (15), we can design the experimental pulse sequence for the realization of the $U_S(\pi,\theta,0)$ gate, as shown in Fig. 5(a). Similarly, for the realization of a composite gate with $N = 2$, $U_S(\pi,\theta,0) = [U_S(\pi/2,\theta,0)]^2$, where

$$U_S(\pi/2,\theta,0) = e^{-i\mathcal{H}_S(\Omega,\theta,0;3\pi/2)(\tau/2)}e^{-i\mathcal{H}_S(\Omega,\theta,0;0)(\tau/2)}, \quad \text{(A4)}$$

with $\mathcal{H}_S(\Omega,\theta,0;3\pi/2) = \Omega[-\cos(\theta/2)(X_1Y_2 - Y_1X_2) + \sin(\theta/2)(X_2Y_3 - Y_2X_3)]/2$. Figure 5(b) shows the whole experimental pulse sequence for $U_S(\pi,\theta,0)$ in the realization of the composite-gate scheme with $N = 2$.

For the experimental realization of the two-logical-qubit gate $U_T(\pi/4,0)$, the target Hamiltonian is $\mathcal{H}_T = \Omega'[\cos(\pi/8)(X_3X_4 + Y_3Y_4) + \sin(\pi/8)(X_3X_6 + Y_3Y_6)]/2$, which is the same as the Hamiltonian for the holonomic Hadamard gate, except for the qubit labeling. Therefore, it can also be implemented by the pulse sequence shown in Fig. 5.

APPENDIX B: QUANTUM-PROCESS TOMOGRAPHY IN THE DFS

In the maintext, we follow the standard QPT method [48] to experimentally reconstruct χ matrices in the logical-qubit subspace for holonomic operations. The goal of QPT is to determine a fixed set of operation elements $\{\tilde{E}_i\}$ for a quantum channel $\mathcal{E}$: $\mathcal{E}(\rho) = \sum_{mn}\chi_{mn}\tilde{E}_m\rho\tilde{E}_n$. Let ρ_j $(1 \le j \le d^2)$ be a fixed, linearly independent basis for the space of $d \times d$ matrices. Each $\mathcal{E}(\rho_j)$ may be expressed as a linear combination of the basis states $\mathcal{E}(\rho_j) = \sum_k \lambda_{jk}\rho_k$. Given that an input state ρ_i and $\{\tilde{E}_i\}$ are known, one can determine the action of $\tilde{E}_m\rho_j\tilde{E}_n = \sum_k \beta_{jk}^{mn}\rho_k$, where β_{jk}^{mn} are complex numbers that can be determined by standard algorithms. Thus, $\sum_k\sum_{mn}\chi_{mn}\beta_{jk}^{mn}\rho_k = \sum_k\lambda_{jk}\rho_k$. From the linear independence of the ρ_k, it follows that $\sum_{mn}\beta_{jk}^{mn}\chi_{mn} = \lambda_{jk}$ for each k. Finally, one can determine χ_{mn} given the known values of β_{jk}^{mn} and λ_{jk} using standard methods of linear algebra.

For single-logical-qubit gates, the fixed set of operation elements $\{\tilde{E}_i\}$ can be

$$\tilde{E}_0 = I_L, \quad \tilde{E}_1 = X_L, \quad \tilde{E}_2 = -iY_L, \quad \tilde{E}_3 = Z_L, \quad \text{(B1)}$$

where $I_L = |0\rangle_L\langle 0| + |1\rangle_L\langle 1|$, $X_L = |0\rangle_L\langle 1| + |1\rangle_L\langle 0|$, $Y_L = i|0\rangle_L\langle 1| - i|1\rangle_L\langle 0|$, and $Z_L = |0\rangle_L\langle 0| - |1\rangle_L\langle 1|$ in the DFS.

TABLE II. Distances of all experimental final states after nonadiabatic Holonomic quantum gates. Superscripts X1 and H1 denote NOT and Hadamard gates, respectively, in the single-loop scheme, superscripts X2 and H2 denote NOT and Hadamard gates, respectively, in the composite scheme, and superscript 2 denotes a two-logical-qubit gate. Subscripts F and L denote the three-physical-qubit space and the logical-qubit subspace, respectively.

Order	Initial state	D_F^{X1}	D_L^{X1}	D_F^{X2}	D_L^{X2}	D_F^{H1}	D_L^{H1}	D_F^{H2}	D_L^{H2}	D_F^2	D_L^2
1	$\|0\rangle_L$	0.243	0.187	0.244	0.171	0.289	0.198	0.259	0.184		
2	$\|1\rangle_L$	0.275	0.191	0.228	0.165	0.285	0.191	0.251	0.185		
3	$\|+\rangle_L$	0.305	0.225	0.287	0.237	0.319	0.233	0.278	0.218		
4	$\|-\rangle_L$	0.259	0.160	0.278	0.203	0.254	0.195	0.250	0.179		
5	$\|00\rangle_L$									0.289	0.221
6	$\|01\rangle_L$									0.279	0.231
7	$\|10\rangle_L$									0.278	0.249
8	$\|11\rangle_L$									0.256	0.228
9	$(\|00\rangle_L+\|01\rangle_L)/\sqrt{2}$									0.307	0.255
10	$(\|10\rangle_L+\|11\rangle_L)/\sqrt{2}$									0.268	0.235
11	$(\|00\rangle_L+i\|01\rangle_L)/\sqrt{2}$									0.236	0.208
12	$(\|10\rangle_L+i\|11\rangle_L)/\sqrt{2}$									0.242	0.215
13	$(\|00\rangle_L+\|10\rangle_L)/\sqrt{2}$									0.286	0.243
14	$(\|01\rangle_L+\|11\rangle_L)/\sqrt{2}$									0.263	0.210
15	$(\|00\rangle_L+i\|10\rangle_L)/\sqrt{2}$									0.250	0.214
16	$(\|01\rangle_L+i\|11\rangle_L)/\sqrt{2}$									0.231	0.171
17	$(\|00\rangle_L+\|01\rangle_L+\|10\rangle_L+\|11\rangle_L)/2$									0.276	0.212
18	$(\|00\rangle_L+i\|01\rangle_L+\|10\rangle_L+i\|01\rangle_L)/2$									0.263	0.230
19	$(\|00\rangle_L+\|01\rangle_L+i\|10\rangle_L+i\|11\rangle_L)/2$									0.287	0.259
20	$(\|00\rangle_L+i\|01\rangle_L+i\|10\rangle_L-\|11\rangle_L)/2$									0.275	0.240

There are 12 parameters, specified by χ_1. We prepare four input states as

$$\{|0\rangle_L, |1\rangle_L, (|0\rangle_L+|1\rangle_L)/\sqrt{2}, (|0\rangle_L+i|1\rangle_L)/\sqrt{2}\},$$

and the final states through a quantum channel $\mathcal{E}$ are

$$\begin{aligned}
\rho_1' &= \mathcal{E}(|0\rangle_L\langle 0|),\\
\rho_4' &= \mathcal{E}(|1\rangle_L\langle 1|),\\
\rho_2' &= \mathcal{E}(|+\rangle_L\langle +|) + i\mathcal{E}(|-\rangle_L\langle -|) - (1+i)(\rho_1'+\rho_4')/2,\\
\rho_3' &= \mathcal{E}(|+\rangle_L\langle +|) - i\mathcal{E}(|-\rangle_L\langle -|) - (1-i)(\rho_1'+\rho_4')/2,
\end{aligned}$$

which can be reconstructed with use of quantum-state tomography (i.e., experimental density matrices for three physical qubits). To illustrate the behaviors of quantum gates in the logical-qubit subspace, we extract the matrix elements only in DFS S_1 to form $\rho_m'^L = \sum_{i',j'\in\{100,001\}} c_{i'j'}|i'\rangle\langle j'|$ from the three-qubit state $\rho_m' = \sum_{i,j\in\{000,001,\ldots,111\}} c_{ij}|i\rangle\langle j|$. The experimentally reconstructed results for the initial and final states in the three-physical-qubit space are shown in Figs. 6 and 7, respectively, where the elements in the logical-qubit subspace are marked as the dark bars. We calculate the corresponding distances of $\rho_m'^L$ from the theoretical ones, listed in Tables I and II. From the experimental $\rho_m'^L$, we obtain the χ matrices for single-logical-qubit gates in the DFS as

$$\chi_1^L = \Lambda_1^L \begin{pmatrix} \rho_1'^L & \rho_2'^L \\ \rho_3'^L & \rho_4'^L \end{pmatrix} \Lambda_1^L, \tag{B2}$$

with

$$\Lambda_1 = \frac{1}{2}\begin{pmatrix} I_L & X_L \\ X_L & -I_L \end{pmatrix}. \tag{B3}$$

For two-logical-qubit gates, we prepare 16 initial states $|\psi_{nm}\rangle = |n\rangle \otimes |m\rangle$, where $|n\rangle, |m\rangle \in \{|0\rangle_\mathrm{L}, |1\rangle_\mathrm{L}, (|0\rangle_\mathrm{L} + |1\rangle_\mathrm{L})/\sqrt{2}, (|0\rangle_\mathrm{L} + i|1\rangle_\mathrm{L})/\sqrt{2}\}$, and measure the final states through the two-logical-qubit quantum channel: $\rho_{mn}' = \mathcal{E}(\rho_{mn} = |\psi_{nm}\rangle\langle\psi_{nm}|)$. As for the case for single-logical-qubit gates, we reconstruct the physical-qubit state ρ_{mn}' and then extract the elements in DFS S_2 to form $\rho_{mn}'^L$. From the experimental $\rho_{mn}'^L$, the χ matrices for two-logical-qubit gates in DFS are obtained as

$$\chi_2 = \Lambda_2^L \overline{\rho}'^L \Lambda_2^L, \tag{B4}$$

where $\Lambda_2^L = \Lambda_1^L \otimes \Lambda_1^L$, and

$$\overline{\rho}'^L = P_L^T \begin{pmatrix} \rho_{11}'^L & \rho_{12}'^L & \rho_{13}'^L & \rho_{14}'^L \\ \rho_{21}'^L & \rho_{22}'^L & \rho_{23}'^L & \rho_{24}'^L \\ \rho_{31}'^L & \rho_{32}'^L & \rho_{33}'^L & \rho_{34}'^L \\ \rho_{41}'^L & \rho_{42}'^L & \rho_{43}'^L & \rho_{44}'^L \end{pmatrix} P_L, \tag{B5}$$

where $P_L = I_L \otimes [(\rho^L_{11} + \rho^L_{23} + \rho^L_{32} + \rho^L_{44}) \otimes I_L]$ and P^T_L is the transposition of P_L.

APPENDIX C: ERROR ANALYSIS

Tables I and II shows the distances of all initial states experimentally prepared in Figs. 6 and 7 from the theoretical ones. If we input these experimental initial states into an ideal quantum channel, the distances of the reconstructed χ matrices in the logical-qubit subspace by ideal QPT are around 0.148 and 0.167 for the single-logical qubit gates and the two-logical-qubit gates, respectively. According to the experimental signal-to-noise ratio, we perform a numerical simulation by generating white Gaussian noise on the measurements, which leads to an error of around 0.026. Consequently, the errors for the χ-matrix QPT come mainly from the imperfection of the initial states, as well as that of quantum-channel χ reconstructed (e.g., the nonadiabatic holonomic quantum gates). We also find that the gate distance for the two-logical-qubit gate is larger than that for the single-logical-qubit case. This is because that the two logical qubits have a larger Hilbert subspace than the single logical qubit, and a larger Hilbert space results in more errors in the matrix elements.

[1] M. V. Berry, Quantal phase factors accompanying adiabatic changes, Proc. R. Soc. London A **392**, 45 (1984).
[2] F. Wilczek and A. Zee, Appearance of Gauge Structure in Simple Dynamical Systems, Phys. Rev. Lett. **52**, 2111 (1984).
[3] Y. Aharonov and J. Anandan, Phase Change during a Cyclic Quantum Evolution, Phys. Rev. Lett. **58**, 1593 (1987).
[4] P. Solinas, P. Zanghì, and N. Zanghì, Robustness of non-Abelian holonomic quantum gates against parametric noise, Phys. Rev. A **70**, 042316 (2004).
[5] S.-L. Zhu and P. Zanardi, Geometric quantum gates that are robust against stochastic control errors, Phys. Rev. A **72**, 020301(R) (2005).
[6] J. T. Thomas, M. Lababidi, and M. Z. Tian, Robustness of single-qubit geometric gate against systematic error, Phys. Rev. A **84**, 042335 (2011).
[7] P. Solinas, M. Sassetti, T. Truini, and N. Zanghì, On the stability of quantum holonomic gates, New J. Phys. **14**, 093006 (2012).
[8] M. Johansson, E. Sjoqvist, L. M. Andersson, M. Ericsson, B. Hessmo, K. Singh, and D. M. Tong, Robustness of nonadiabatic holonomic gates, Phys. Rev. A **86**, 062322 (2012).
[9] E. Sjöqvist, Trend: A new phase in quantum computation, Physics **1**, 35 (2008).
[10] P. Zanardi and M. Rasetti, Holonomic quantum computation, Phys. Lett. A **264**, 94 (1999).
[11] J. Pachos, P. Zanardi, and M. Rasetti, Non-Abelian Berry connections for quantum computation, Phys. Rev. A **61**, 010305 (1999).
[12] L. M. Duan, J. I. Cirac, and P. Zoller, Geometric manipulation of trapped ions for quantum computation, Science **292**, 1695 (2001).
[13] V. V. Albert, C. Shu, S. Krastanov, C. Shen, R.-B. Liu, Z.-B. Yang, R. J. Schoelkopf, M. Mirrahimi, M. H. Devoret, and L. Jiang, Holonomic Quantum Control with Continuous Variable Systems, Phys. Rev. Lett. **116**, 140502 (2016).
[14] W. Xiang-Bin and M. Keiji, Nonadiabatic Conditional Geometric Phase Shift with NMR, Phys. Rev. Lett. **87**, 097901 (2001).
[15] S.-L. Zhu and Z. D. Wang, Implementation of Universal Quantum Gates based on Nonadiabatic Geometric Phases, Phys. Rev. Lett. **89**, 097902 (2002).
[16] E. Sjöqvist, D. M. Tong, L. Mauritz Andersson, B. Hessmo, M. Johansson, and K. Singh, Non-adiabatic holonomic quantum computation, New J. Phys. **14**, 103035 (2012).
[17] G. F. Xu, C. L. Liu, P. Z. Zhao, and D. M. Tong, Nonadiabatic holonomic gates realized by a single-shot implementation, Phys. Rev. A **92**, 052302 (2015).
[18] E. Herterich and E. Sjöqvist, Single-loop multiple-pulse nonadiabatic holonomic quantum gates, Phys. Rev. A **94**, 052310 (2016).
[19] Z.-Y. Xue, F.-L. Gu, Z.-P. Hong, Z.-H. Yang, D.-W. Zhang, Y. Hu, and J. Q. You, Nonadiabatic Holonomic Quantum Computation with Dressed-State Qubits, Phys. Rev. Appl. **7**, 054022 (2017).
[20] G. Feng, G. Xu, and G. Long, Experimental Realization of Nonadiabatic Holonomic Quantum Computation, Phys. Rev. Lett. **110**, 190501 (2013).
[21] H. Li, L. Yang, and G. Long, Experimental realization of single-shot nonadiabatic holonomic gates in nuclear spins, Sci. China: Phys. Mech. Astron. **60**, 080311 (2017).
[22] A. A. Abdumalikov, J. M. Fink, K. Juliusson, M. Pechal, S. Berger, A. Wallraff, and S. Filipp, Experimental realization of non-Abelian non-adiabatic geometric gates, Nature (London) **496**, 482 (2013).
[23] Y. Xu, W. Cai, Y. Ma, X. Mu, L. Hu, T. Chen, H. Wang, Y. P. Song, Z.-Y. Xue, Z.-Q. Yin, and L. Sun, Single-Loop Realization of Arbitrary Nonadiabatic Holonomic Single-Qubit Quantum Gates in a Superconducting Circuit, Phys. Rev. Lett. **121**, 110501 (2018).
[24] D. J. Egger, M. Ganzhorn, G. Salis, A. Fuhrer, P. Müller, P. Kl. Barkoutsos, N. Moll, I. Tavernelli, and S. Filipp, Entanglement Generation in Superconducting Qubits Using Holonomic Operations, Phys. Rev. Appl. **11**, 014017 (2019).
[25] C. Zu, W.-B. Wang, L. He, W.-G. Zhang, C.-Y. Dai, F. Wang, and L.-M. Duan, Experimental realization of universal geometric quantum gates with solid-state spins, Nature (London) **514**, 72 (2014).
[26] S. Arroyo-Camejo, A. Lazariev, S. W. Hell, and G. Balasubramanian, Room temperature high-fidelity holonomic single-qubit gate on a solid-state spin, Nat. Commun. **5**, 4870 (2014).
[27] Y. Sekiguchi, N. Niikura, R. Kuroiwa, H. Kano, and H. Kosaka, Optical holonomic single quantum gates with a geometric spin under a zero field, Nat. Photonics **11**, 309 (2017).

[28] B. B. Zhou, P. C. Jerger, V. O. Shkolnikov, F. J. Heremans, G. Burkard, and D. D. Awschalom, Holonomic Quantum Control by Coherent Optical Excitation in Diamond, Phys. Rev. Lett. **119**, 140503 (2017).
[29] N. Ishida, T. Nakamura, T. Tanaka, S. Mishima, H. Kano, R. Kuroiwa, Y. Sekiguchi, and H. Kosaka, Universal holonomic single quantum gates over a geometric spin with phase-modulated polarized light, Opt. Lett. **43**, 2380 (2018).
[30] K. Nagata, K. Kuramitani, Y. Sekiguchi, and H. Kosaka, Universal holonomic quantum gates over geometric spin qubits with polarised microwaves, Nat. Commun. **9**, 3227 (2018).
[31] L.-M. Duan and G.-C. Guo, Preserving Coherence in Quantum Computation by Pairing Quantum Bits, Phys. Rev. Lett. **79**, 1953 (1997).
[32] P. Zanardi and M. Rasetti, Noiseless Quantum Codes, Phys. Rev. Lett. **79**, 3306 (1997).
[33] D. A. Lidar, I. L. Chuang, and K. B. Whaley, Decoherence-Free Subspaces for Quantum Computation, Phys. Rev. Lett. **81**, 2594 (1998).
[34] G. F. Xu, J. Zhang, D. M. Tong, E. Sjöqvist, and L. C. Kwek, Nonadiabatic Holonomic Quantum Computation in Decoherence-Free Subspaces, Phys. Rev. Lett. **109**, 170501 (2012).
[35] J. Zhang, L.-C. Kwek, E. Sjöqvist, D. M. Tong, and P. Zanardi, Quantum computation in noiseless subsystems with fast non-Abelian holonomies, Phys. Rev. A **89**, 042302 (2014).
[36] G. Xu and G. Long, Universal nonadiabatic geometric gates in two-qubit decoherence-free subspaces, Sci. Rep. **4**, 6814 (2014).
[37] Z.-T. Liang, Y.-X. Du, W. Huang, Z.-Y. Xue, and H. Yan, Nonadiabatic holonomic quantum computation in decoherence-free subspaces with trapped ions, Phys. Rev. A **89**, 062312 (2014).
[38] J. Zhou, W.-C. Yu, Y.-M. Gao, and Z.-Y. Xue, Cavity QED implementation of non-adiabatic holonomies for universal quantum gates in decoherence-free subspaces with nitrogen-vacancy centers, Opt. Express **89**, 14027 (2015).
[39] Z.-Y. Xue, J. Zhou, and Z. D. Wang, Universal holonomic quantum gates in decoherence-free subspace on superconducting circuits, Phys. Rev. A **92**, 022320 (2015).
[40] Z.-Y. Xue, J. Zhou, Y.-M. Chu, and Y. Hu, Nonadiabatic holonomic quantum computation with all-resonant control, Phys. Rev. A **94**, 022331 (2016).
[41] P. Z. Zhao, G. F. Xu, Q. M. Ding, E. Sjöqvist, and D. M. Tong, Single-shot realization of nonadiabatic holonomic quantum gates in decoherence-free subspaces, Phys. Rev. A **95**, 062310 (2017).
[42] Z.-P. Hong, B.-J. Liu, J.-Q. Cai, X.-D. Zhang, Y. Hu, Z. D. Wang, and Z.-Y. Xue, Implementing universal nonadiabatic holonomic quantum gates with transmons, Phys. Rev. A **97**, 022332 (2018).
[43] G. F. Xu, P. Z. Zhao, T. H. Xing, E. Sjöqvist, and D. M. Tong, Composite nonadiabatic holonomic quantum computation, Phys. Rev. A **95**, 032311 (2017).
[44] T. Chen and Z.-Y. Xue, Nonadiabatic Geometric Quantum Computation with Parametrically Tunable Coupling, Phys. Rev. Appl. **10**, 054051 (2018).
[45] S. B. Zheng, C. P. Yang, and F. Nori, Comparison of the sensitivity to systematic errors between nonadiabatic non-Abelian geometric gates and their dynamical counterparts, Phys. Rev. A **93**, 032313 (2016).
[46] J. Jing, C.-H. Lam, and L.-A. Wu, Non-Abelian holonomic transformation in the presence of classical noise, Phys. Rev. A **95**, 012334 (2017).
[47] X. Peng, X. Zhu, X. Fang, M. Feng, K. Gao, X. Yang, and M. Liu, Preparation of pseudo-pure states by line-selective pulses in nuclear magnetic resonance, Chem. Phys. Lett. **340**, 509 (2001).
[48] I. L. Chuang and M. A. Nielsen, Prescription for experimental determination of the dynamics of a quantum black box, J. Mod. Opt. **44**, 2455 (1997).
[49] J.-S. Lee, The quantum state tomography on an NMR system, Phys. Lett. A **305**, 349 (2002).
[50] G. Wang, Property testing of unitary operators, Phys. Rev. A **84**, 052328 (2011).
[51] A. Shabani and D. A. Lidar, Theory of initialization-free decoherence-free subspaces and subsystems, Phys. Rev. A **72**, 042303 (2005).